

Cite this: *Chem. Sci.*, 2023, **14**, 8507

All publication charges for this article have been paid for by the Royal Society of Chemistry

Received 25th June 2023

Accepted 14th July 2023

DOI: 10.1039/d3sc03213b

rsc.li/chemical-science

## Introduction

Direct air capture (DAC) of  $\text{CO}_2$  has emerged as a promising carbon negative approach to achieving carbon neutrality.<sup>1–5</sup> However, the extremely low concentration of  $\text{CO}_2$  in the air ( $\sim 410$  ppm) presents a significant challenge. Various solid adsorption materials such as zeolite, activated carbon, porous silicon, coordination polymers, metal-organic frameworks (MOFs), and covalent organic frameworks (COFs) have been explored for  $\text{CO}_2$  capture.<sup>6–20</sup> MOFs, with their diverse structures and post-modification functionalization,<sup>21</sup> show potential for  $\text{CO}_2$  adsorption, but are still challenging for low-concentration  $\text{CO}_2$  capture, especially for DAC. Currently, only a few ultra-microporous MOFs and bioinspired MOFs are capable of capturing ultra-low concentrations of  $\text{CO}_2$ .<sup>22–31</sup> One of the most widely studied strategies for achieving low-concentration  $\text{CO}_2$  adsorption is amine modification, which has ultra-strong affinity for  $\text{CO}_2$  molecules.<sup>32–37</sup> However, amine adsorption suffers from low adsorption kinetics, low amine efficiency and loss of amines, limiting its practical application.<sup>38,39</sup> Therefore, the development of non-amine modified low-concentration  $\text{CO}_2$  adsorption MOFs-based materials is necessary. Zr-based MOFs with secondary building units (SBUs) show promise due to their

SBUs and high coordination numbers.<sup>40</sup> Controlled etching of these MOFs exposes more M-OH sites, and the microporous environment of MOFs enhances local  $\text{CO}_2$  enrichment and capture, but exploration in this area is still limited.

In this study, we synthesized a series of controlled alkali-etched MOF-808-X ( $X: 0.04\text{--}0.10$ ) materials with enhanced low-concentration  $\text{CO}_2$  capture capacity under simulated air conditions compared to the pristine MOF-808. Among these materials, MOF-808-0.07 exhibited a  $\text{CO}_2$  capture capacity of  $0.21 \text{ mmol g}^{-1}$  under simulated air conditions, which is 70 times higher than that of the pristine MOF-808. Additionally, MOF-808-0.07 displayed excellent stability over 50 cycles of adsorption and desorption. *In situ* DRIFTS and  $^{13}\text{C}$  CP-MAS ssNMR analysis revealed that the increased low-concentration  $\text{CO}_2$  capture capacity is attributed to the formation of a stable six-membered ring structure through the interaction of intramolecular hydrogen bonds between neighbouring Zr-OH sites in the micro-mesoporous environment of MOF-808-X.

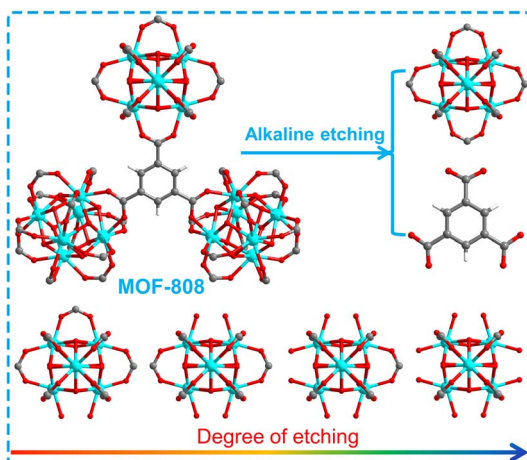
## Results and discussion

MOF-808 was synthesized according to the reported method.<sup>40,41</sup> And MOF-808-X ( $X: 0.04\text{--}0.10$ ) series were prepared by various degrees of alkali etching of MOF-808 (Scheme 1). In Fig. 1a, the FT-IR analysis of these samples reveals that the infrared absorption peaks at  $1630$  and  $1400\text{--}1600 \text{ cm}^{-1}$ , which correspond to the stretching vibration peak of  $\text{C}=\text{O}$  and the benzene ring, respectively, display varying degrees of weakening. This

State Key Laboratory of Catalysis, Dalian National Laboratory for Clean Energy, Dalian Institute of Chemical Physics, Chinese Academy of Sciences, Dalian 116023, China. E-mail: canli@dicp.ac.cn

† Electronic supplementary information (ESI) available. See DOI: <https://doi.org/10.1039/d3sc03213b>





**Scheme 1** Schematic diagram of degree of etching for MOF-808 and series of MOF-808-X (X: 0.04–0.10).

suggests that the benzene ring in MOF-808 has undergone degradation to different extents. In Fig. 1b, the powder X-ray diffraction (PXRD) patterns of the as-synthesized MOF-808 are shown, which match well with the simulated PXRD pattern obtained from single crystal analysis.<sup>40</sup> However, the PXRD peaks of the MOF-808-X (X: 0.04–0.10) series gradually weaken with increasing etching degree, until all XRD diffraction peaks disappear. Scanning electron microscopy (SEM) images of the as-synthesized MOF-808 exhibit octahedral morphology (Fig. S1a†), consistent with previous literature reports. The alkali-etched MOF-808-X (X: 0.04–0.10) series show almost the same morphology as MOF-808 with varying degrees of etching (Fig. S1b–f†).

X-ray photoelectron spectroscopy (XPS) analyses were conducted to investigate the electronic structure of MOF-808 and MOF-808-X (X: 0.04–0.07) series (Fig. 1c). In Fig. 1d, the C 1s high-resolution spectrum of MOF-808 and MOF-808-X series displays two distinct binding energy peaks at 284.8 and 288.5 eV, corresponding to the binding energy peaks of C–C and C–O. The O 1s high-resolution spectrum of MOF-808 in Fig. 1e shows a binding energy peak of C–O–Zr bond at 532.5 eV. However, a new binding energy peak appeared in the O 1s HR-XPS spectrum at 530.5 eV, which gradually increased with the increase of the alkali etching degree of MOF-808, and the new binding energy peak was attributed to the Zr–OH generated by alkali etching. Moreover, it is obvious from Fig. 1f that the binding energy peak of Zr 3d is shifted towards a lower binding energy in MOF-808-X series compared to the pristine MOF-808. These results suggest that electron-donating groups exist on the Zr site.

$\text{N}_2$  adsorption and desorption isotherms were employed to further characterize the pore structure and BET surface area of MOF-808 and MOF-808-X series. The isotherms of these materials exhibit a typical type I adsorption pattern (as shown in Fig. S2†), indicating the presence of micro-mesoporous structure. The BET specific surface area of MOF-808 was found to be  $1614 \text{ m}^2 \text{ g}^{-1}$ , whereas for MOF-808-X (X: 0.04–0.07) series, the BET specific surface area gradually decreases with the increase in the degree of etching and is found to be 300, 229, 225, 221, and  $144 \text{ m}^2 \text{ g}^{-1}$ , respectively. This suggests that the BET surface area changes as the degree of etching increases due to the gradual collapse of the MOF-808 framework.

Due to the presence of numerous Zr–OH sites in the MOF-808-X series, we were prompted to investigate the  $\text{CO}_2$  adsorption characteristics of these materials. As shown in Fig. 2a, the

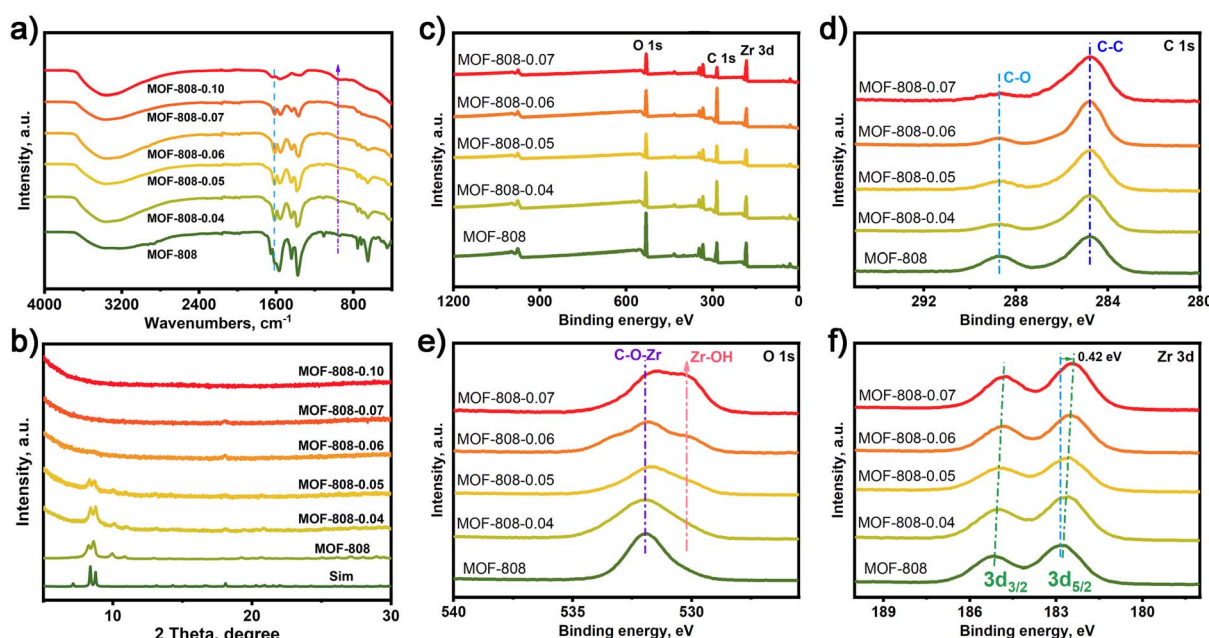


**Fig. 1** (a) FT-IR spectra, (b) PXRD patterns and (c–f) XPS survey, and high-resolution XPS spectra of the C 1s, O 1s, and Zr 3d of MOF-808 and MOF-808-X (X: 0.04–0.1).



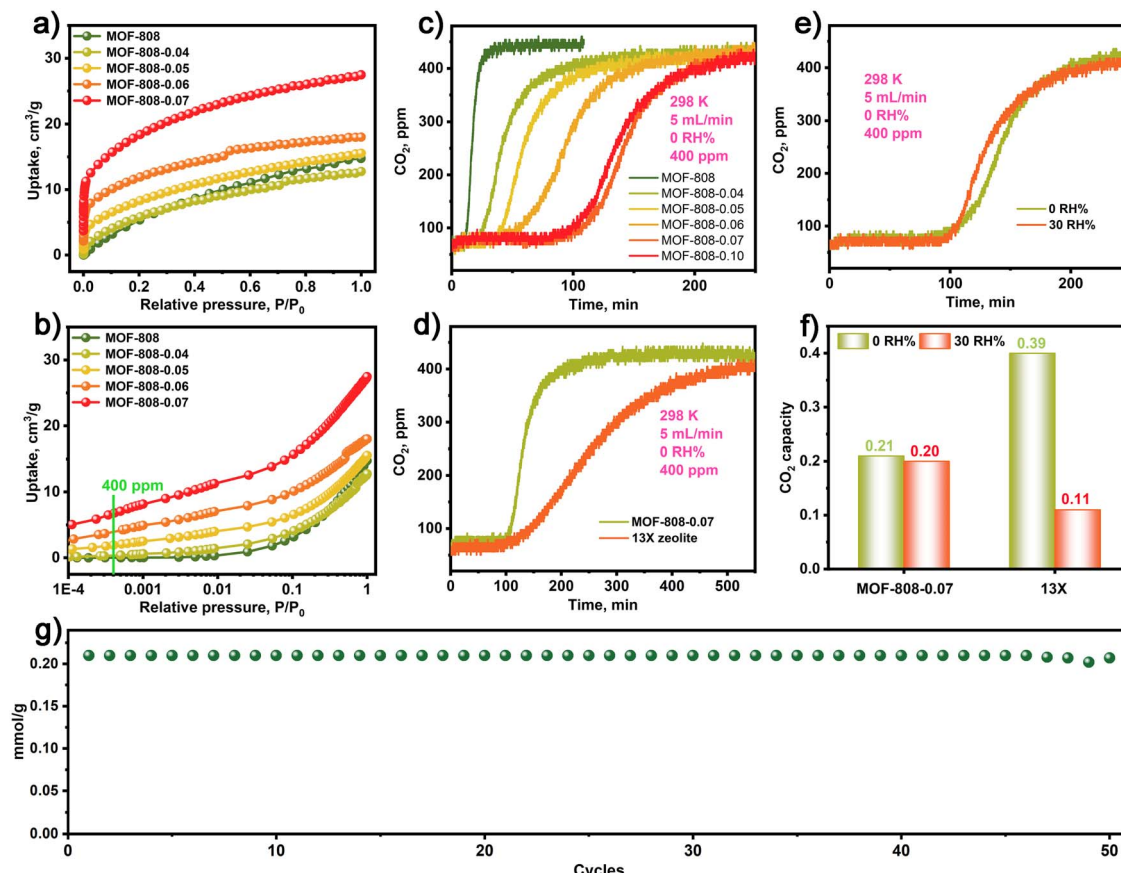


Fig. 2 (a) and (b)  $\text{CO}_2$  adsorption isotherm for MOF-808 and MOF-808-X ( $X: 0.04\text{--}0.07$ ) series. The dynamic  $\text{CO}_2$  breakthrough curves for MOF-808 and MOF-808-X ( $X: 0.04\text{--}0.07$ ) series (c) and 13X zeolite under dry conditions (d). (e) The dynamic  $\text{CO}_2$  breakthrough curves for MOF-808-0.07 at 0 and 30 RH%. (f) Comparison of  $\text{CO}_2$  capture capacity for MOF-808-0.07 and 13X zeolite at 0 and 30 RH%, respectively. (g) The cycling stability of  $\text{CO}_2$  capture for MOF-808-0.07.

$\text{CO}_2$  adsorption isotherms of the MOF-808-X series demonstrate improved  $\text{CO}_2$  adsorption at low pressures compared to the pristine MOF-808. Particularly, the MOF-808-X series materials with Zr-OH sites exhibit a strong affinity for  $\text{CO}_2$  at low concentrations, as evidenced by the steepness of the  $\text{CO}_2$  adsorption isotherms and the attainment of a plateau at very low pressures. Further analysis of the  $\text{CO}_2$  adsorption behaviour (Fig. 2b) within a low-pressure range of 400 ppm reveals that MOF-808-0.07 exhibits a high  $\text{CO}_2$  uptake of  $0.28 \text{ mmol g}^{-1}$ , which is comparable to the values obtained for MOF-808-0.04 ( $0.01 \text{ mmol g}^{-1}$ ), MOF-808-0.05 ( $0.08 \text{ mmol g}^{-1}$ ), MOF-808-0.06 ( $0.16 \text{ mmol g}^{-1}$ ), and the pristine MOF-808 ( $0.008 \text{ mmol g}^{-1}$ ). This highlights the significantly enhanced  $\text{CO}_2$  uptake and the interactions between  $\text{CO}_2$  and Zr-OH sites in the MOF-808-X series materials compared to the pristine MOF-808. Additionally, the MOF-808-X series exhibits excellent thermal stability up to  $200^\circ\text{C}$  (Fig. S3†).

The dynamic  $\text{CO}_2$  capture performance of MOF-808 and MOF-808-X series were assessed in a fixed-bed reactor packed with a column of simulated ambient air (400 ppm  $\text{CO}_2$  and argon as balance gas) under flow conditions ( $5 \text{ mL min}^{-1}$ ) at  $298 \text{ K}$ . The detailed experimental procedure is provided in the ESI.† Fig. 2c depicts the short-term  $\text{CO}_2$  breakthrough process of

pristine MOF-808 in simulated dry air conditions (0 RH%), resulting in low  $\text{CO}_2$  capture capacities of  $0.003 \text{ mmol g}^{-1}$ . In contrast, MOF-808-X ( $X: 0.04\text{--}0.10$ ) series exhibited long-term dynamic  $\text{CO}_2$  breakthrough processes with enhanced  $\text{CO}_2$  capture capacity compared to the pristine MOF-808. The dynamic  $\text{CO}_2$  capture capacity of MOF-808-X ( $X: 0.04\text{--}0.10$ ) series under simulated dry air conditions were  $0.06$ ,  $0.09$ ,  $0.13$ ,  $0.21$ , and  $0.205 \text{ mmol g}^{-1}$ , respectively. Notably, the MOF-808-0.07 demonstrated the highest  $\text{CO}_2$  capture capacity, which is a 70-fold increase in  $\text{CO}_2$  uptake capacity compared to the pristine MOF-808. Although the MOF-808-X series exhibited lower  $\text{CO}_2$  capture capacity than the 13X zeolite ( $0.39 \text{ mmol g}^{-1}$ ) under simulated dry air conditions, they demonstrated faster adsorption kinetics than 13X zeolite, as illustrated by the sharper breakthrough profile for MOF-808-0.07 compared to 13X (Fig. 2e). Additionally, Fig. 2d indicates that MOF-808-0.07 exhibited almost the same  $\text{CO}_2$  breakthrough curves under simulated dry and humid air conditions (0 and 30 RH%). In contrast, the 13X zeolite in Fig. 2f exhibited significantly reduced  $\text{CO}_2$  capture capacity under humid air conditions (30 RH%), indicating that MOF-808 has higher moisture resistance. Moreover, Fig. 2g demonstrates that MOF-808-0.07 exhibited stable  $\text{CO}_2$  capture performance with minimal losses after 50

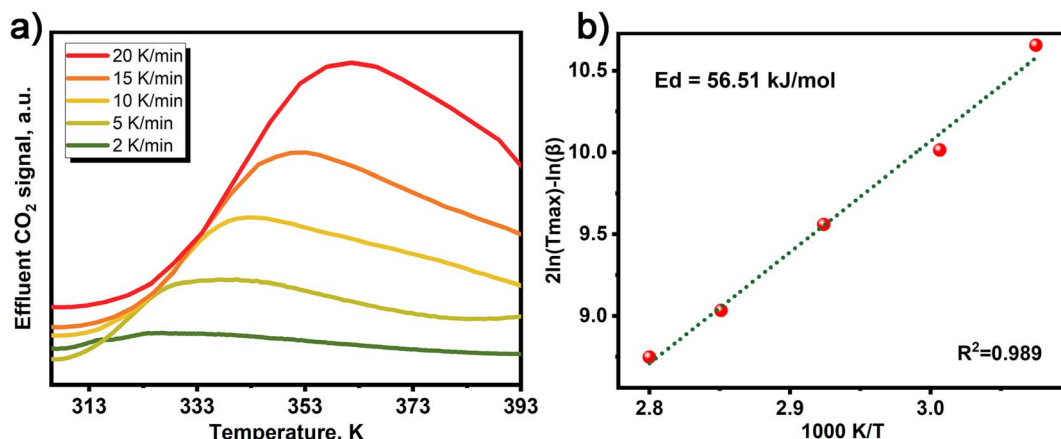


Fig. 3 (a) TPD results for CO<sub>2</sub> desorption from MOF-808-0.07 in dry conditions after being saturated with CO<sub>2</sub> from a gas stream of 400 ppm CO<sub>2</sub>. (b) Microkinetic analysis assuming first order desorption.

cycles (Fig. S4†). In addition, the MOF-808-0.07 after CO<sub>2</sub> capture was evaluated by FT-IR, PXRD, SEM, XPS and N<sub>2</sub> adsorption and desorption isotherms, all results show the structure integrity for MOF-808-0.07 in CO<sub>2</sub> capture processing (Fig. S5–S9†). The above results indicate that the MOF-808-0.07 has superior CO<sub>2</sub> adsorption–desorption stability.

In order to illustrate the low-concentration CO<sub>2</sub> adsorption process of MOFs containing Zr-SBUs at low concentrations, we

synthesized a series of MOFs with different M-SBUs, including MIL-101-Fe with Fe<sub>3</sub>-SBU cluster, MIL-101-Cr with Cr<sub>3</sub>-SBU cluster, and MIL-125-Ti with Ti<sub>4</sub>-SBU cluster. Through controlled etching, as confirmed by PXRD analysis (Fig. S10†), we obtained MOFs with varying degrees of etching. The dynamic CO<sub>2</sub> capture results revealed that all MOFs with varying degrees of etching exhibited a CO<sub>2</sub> capture process, but their capture capacities were not comparable to that of MOF-

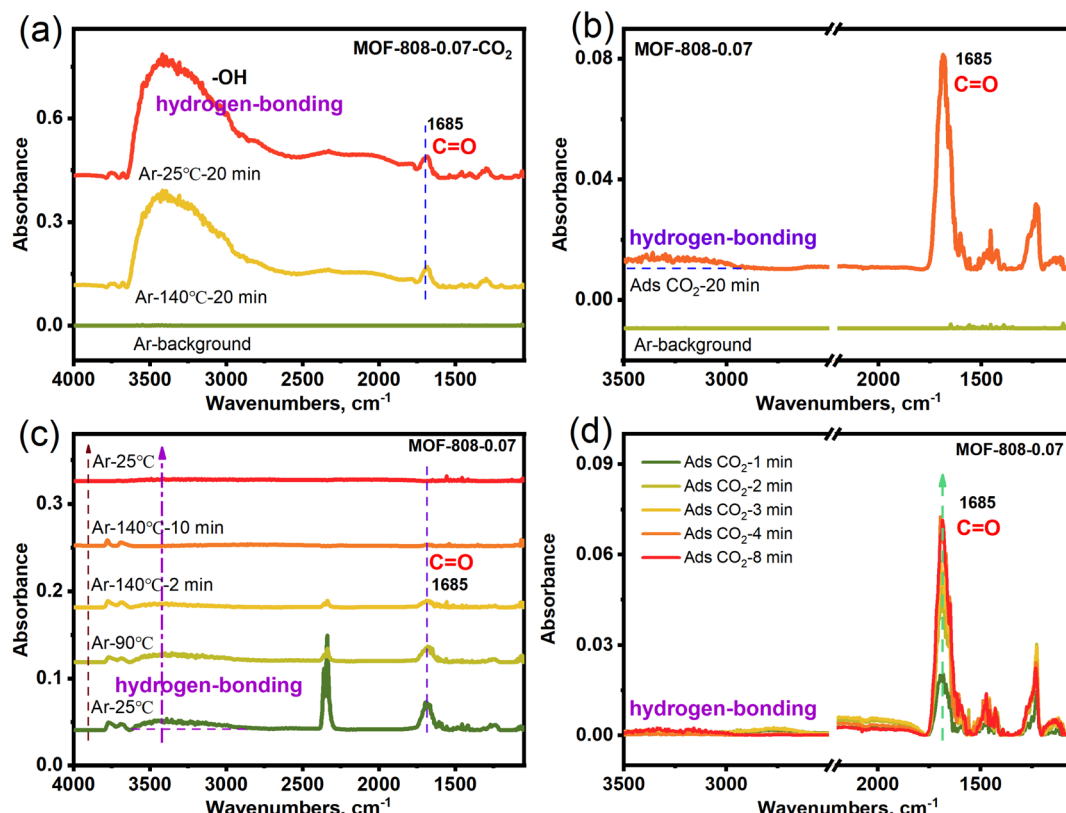


Fig. 4 *In situ* DRIFTS of (a) MOF-808-0.07-CO<sub>2</sub> for desorption CO<sub>2</sub>, (b) MOF-808-0.07 for adsorption CO<sub>2</sub>, (c) MOF-808-0.07-CO<sub>2</sub> for the 2nd desorption CO<sub>2</sub>, (d) MOF-808-0.07 for the 2nd adsorption CO<sub>2</sub>.

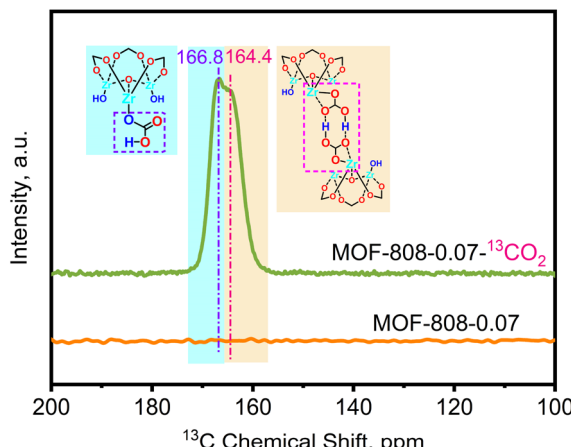


Fig. 5 Stacked plots of solid-state  $^{13}\text{C}$  CP-MAS NMR spectra of MOF-808-0.07 before and after adsorption of  $^{13}\text{CO}_2$ .

808-X with controlled etching with  $\text{Zr}_6$ -SBU cluster (Fig. S11†). This suggests that MOFs with higher coordination numbers exhibit superior  $\text{CO}_2$  capture abilities.

To investigate the desorption kinetics of MOF-808-0.07 in dry air conditions, we employed temperature programmed desorption (TPD) to evaluate its desorption energy. The activation energies of desorption for MOF-808-0.07 were calculated using the method proposed by Cvetanovic and Amenomiya, by measuring the TPD- $\text{CO}_2$  signal at different heating rates, as presented in Fig. 3a and b.<sup>42</sup> Our results demonstrate that MOF-808-0.07 exhibits a higher desorption energy ( $56.51 \text{ kJ mol}^{-1}$ ) than 13X zeolite ( $48.14 \text{ kJ mol}^{-1}$  (ref. 42)) under simulated dry air conditions (Table S1†), indicating that  $\text{CO}_2$  adsorption by MOF-808-0.07 occurs through chemical adsorption.

In order to verify the adsorbed species in  $\text{CO}_2$  capture for MOF-808-0.07, the *in situ* diffuse reflectance infrared Fourier transform spectroscopy (*in situ* DRIFTS) of MOF-808-0.07 with adsorbing  $\text{CO}_2$  in simulated dry air (MOF-808-0.07- $\text{CO}_2$ ) was carried out. Fig. 4a shows two distinct infrared absorption peaks at  $1685$  and  $3000$ – $3600 \text{ cm}^{-1}$  in the *in situ* DRIFTS spectra of MOF-808-0.07- $\text{CO}_2$  after heat treatment ( $140^\circ\text{C}$ ),

corresponding to the stretching vibration peak of  $\text{C}=\text{O}$  ( $-\text{OCO}_2\text{H}$ ), and  $-\text{OH}$  ( $\text{M}-\text{OH}$  with broad peak and hydrogen-bonding), respectively. The results display that the  $\text{CO}_2$  adsorption within the MOF-808-0.07 framework is in the form of bicarbonate species and hydrogen bonding interactions under dry conditions. Furthermore, the heat-treated MOF-808-0.07 is subjected to *in situ*  $\text{CO}_2$  adsorption again in dry conditions, the *in situ* DRIFTS spectra in Fig. 4b show obvious infrared absorption peaks in  $1685$  and  $3000$ – $3500 \text{ cm}^{-1}$  corresponding to the stretching vibration peak of  $\text{C}=\text{O}$  ( $-\text{OCO}_2\text{H}$ ) and hydrogen-bonding. After heat treatment again, the infrared absorption peak of  $\text{C}=\text{O}$  and hydrogen-bonding gradually disappeared again (Fig. 4c), demonstration of the breaking of hydrogen bonding and the successful complete desorption of  $\text{CO}_2$ . Further elucidating the adsorption-desorption stability, the second *in situ*  $\text{CO}_2$  adsorption also showed that the  $\text{C}=\text{O}$  and hydrogen-bonding infrared absorption peak gradually strengthens with various adsorption time (Fig. 4d). As a comparison, the control experiments of pristine MOF-808- $\text{CO}_2$  shows no obvious infrared absorption peak for  $\text{CO}_2$  desorption at  $140^\circ\text{C}$ . And the heat-treated MOF-808 is subjected to *in situ*  $\text{CO}_2$  adsorption again in dry conditions along with various time, the *in situ* DRIFTS spectra show no obvious change in infrared absorption peaks (Fig. S12†). The results show that parent MOF-808 does not have low concentration  $\text{CO}_2$  adsorption capacity. Based on the above *in situ* DRIFTS results, showing that the alkali etched MOF-808-0.07 has enhanced low concentration  $\text{CO}_2$  capture capacity compared to parent MOF-808 under dry air conditions due to the presence of  $\text{Zr}-\text{OH}$  adsorption sites.

To elucidate the formation of  $-\text{OCO}_2\text{H}$  species under dry conditions, solid-state cross-polarization magic-angle spinning (CP-MAS)  $^{13}\text{C}$  NMR experiments were conducted on variant MOF-808-0.07 to investigate the change in chemical species before and after capturing  $^{13}\text{CO}_2$  (isotopic gas). Fig. 5 displays the  $^{13}\text{C}$  CP-MAS ssNMR spectrum of the pristine MOF-808 without adsorbed  $\text{CO}_2$ , showing no observable chemical shifts, indicating complete etching of the carbon framework in MOF-808. Upon adsorption of  $^{13}\text{CO}_2$  under dry conditions, two distinct chemical shifts appeared in the  $^{13}\text{C}$  CP-MAS ssNMR spectrum at  $\delta^{13}\text{C} = 166.8$  and  $164.4 \text{ ppm}$ . Combining these

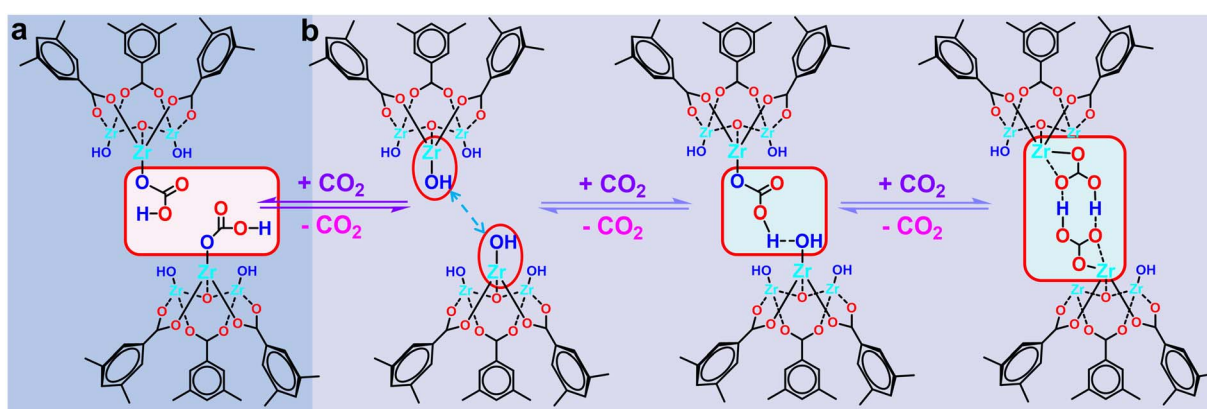


Fig. 6 Proposed low-concentration  $\text{CO}_2$  capture mechanism for MOF-808-X series.



results with the *in situ* DRIFTS data, it can be inferred that these shifts are attributed to  $-\text{OCO}_2\text{H}$  groups and  $-\text{OCO}_2\text{H}$  groups involved in intramolecular hydrogen bonding, respectively.

Based on the above *in situ* DRIFTS and  $^{13}\text{C}$  CP-MAS ssNMR characterizations, we proposed a possible mechanistic of low-concentration  $\text{CO}_2$  capture process in MOF-808 series. (1) When the two Zr-OH sites within the MOF-808-X framework are distanced apart, each Zr-OH site can adsorb one  $\text{CO}_2$  molecule, forming Zr- $\text{O}_2\text{COH}$  species (Fig. 6a). (2) When the neighbouring Zr-OH sites within the MOF-808-X framework are in close proximity. As shown in Fig. 6b, first, a Zr-OH site adsorbs a  $\text{CO}_2$  molecule to form a Zr- $\text{O}_2\text{COH}$  species, and the Zr- $\text{O}_2\text{COH}$  species forms intramolecular hydrogen bonding with the neighbouring Zr-OH site. Subsequently, the neighbouring Zr-OH re-adsorbs a  $\text{CO}_2$  molecule with it to form two opposing Zr- $\text{O}_2\text{COH}$  species, which interact to form a stable six-membered ring structure through the interaction of intramolecular hydrogen bonding to complete an adsorption process.

## Conclusions

In conclusion, we have demonstrated that controlled alkali etching of MOF-808 leads to the formation of MOF-808-X series, which exhibit significantly enhanced low-concentration  $\text{CO}_2$  capture compared to the pristine MOF-808 under dry air conditions. Among the MOF-808-X series, MOF-808-0.07 displays the highest  $\text{CO}_2$  capture capacity of  $0.21 \text{ mmol g}^{-1}$  in simulated dry air conditions, which is 70 times higher than the pristine MOF-808. The desorption kinetics of the MOF-808-0.07 also show higher desorption energy compared to the commonly used 13X zeolite. Our control experiments suggest that MOFs with high coordination numbers show higher  $\text{CO}_2$  capture performance under dry air conditions. Furthermore, *in situ* DRIFTS and  $^{13}\text{C}$  CP-MAS ssNMR results indicate that the enhanced low-concentration  $\text{CO}_2$  capture is due to the formation of a stable six-membered ring structure through intramolecular hydrogen bonds between Zr-OH sites of neighbouring micro-mesoporous environments of MOF-808-X. Overall, these findings suggest the potential of MOF-808-X series as promising materials for low-concentration  $\text{CO}_2$  capture.

## Data availability

The authors declare that all data supporting the findings of this study are available from the corresponding author upon reasonable request.

## Author contributions

Hong Dong: conceptualization, data curation, formal analysis, investigation, funding acquisition, writing – original draft, writing – review & editing. Lihua Li: investigation and formal analysis, Can Li: supervision, funding acquisition, project administration and writing – review & editing.

## Conflicts of interest

There are no conflicts to declare.

## Acknowledgements

This work was supported by the Youth Program of the National Natural Science Foundation of China (No. 22102178), Project funded by China Postdoctoral Science Foundation (No. 2021M693119), and the Special Research Assistant Funding Project of Chinese Academy of Sciences (No. 2021000135). This work was also conducted by the Fundamental Research Center of Artificial Photosynthesis (FReCAP), financially supported by the National Natural Science Foundation of China (NSFC) under Grant No. 22088102. H. Dong would like to thank Shiyanjia Lab for the XPS and  $^{13}\text{C}$  CP-MAS ssNMR analysis.

## Notes and references

- 1 A. Kumar, D. G. Madden, M. Lusi, K. J. Chen, E. A. Daniels, T. Curtin, J. J. Perry and M. J. Zaworotko, *Angew. Chem., Int. Ed.*, 2015, **54**, 14372–14377.
- 2 X. Y. Shi, H. Xiao, H. Azarabadi, J. Z. Song, X. L. Wu, X. Chen and K. S. Lackner, *Angew. Chem., Int. Ed.*, 2020, **59**, 6984–7006.
- 3 C. J. J. Haertel, M. McNutt, M. Ozkan, E. S. P. Aradottir, K. T. Valsaraj, P. R. Sanberg, S. Talati and J. Wilcox, *Chem*, 2021, **7**, 2831–2834.
- 4 X. C. Zhu, W. W. Xie, J. Y. Wu, Y. H. Miao, C. J. Xiang, C. P. Chen, B. Y. Ge, Z. Z. Gan, F. Yang, M. Zhang, D. O'Hare, J. Li, T. S. Ge and R. Z. Wang, *Chem. Soc. Rev.*, 2022, **51**, 6574–6651.
- 5 J. L. Sun, M. Zhao, L. Huang, T. Y. Zhang and Q. Wang, *Curr. Opin. Green Sustainable Chem.*, 2023, **40**, 100752.
- 6 M. Oschatz and M. Antonietti, *Energy Environ. Sci.*, 2018, **11**, 57–70.
- 7 S. Choi, J. H. Drese, P. M. Eisenberger and C. W. Jones, *Environ. Sci. Technol.*, 2011, **45**, 2420–2427.
- 8 A. Ghosh, G. N. Reddy, P. K. M. Siddhique, S. Chatterjee, S. Bhattacharjee, R. Maitra, S. E. Lyubimov, A. V. Arzumanyan, A. Naumkin, A. Bhaumik and B. Chowdhury, *Green Chem.*, 2022, **24**, 1673–1692.
- 9 D. E. F. Oliveira, J. A. O. Chagas, A. L. De Lima and C. J. A. Mota, *Ind. Eng. Chem. Res.*, 2022, **61**, 10522–10530.
- 10 S. M. W. Wilson and F. H. Tezel, *Ind. Eng. Chem. Res.*, 2020, **59**, 8783–8794.
- 11 P. Hu, H. Liu, H. Wang, J. Zhou, Y. Q. Wang and H. B. Ji, *J. Mater. Chem. A*, 2022, **10**, 881–890.
- 12 W. J. Wang, M. Zhouab and D. Q. Yuan, *J. Mater. Chem. A*, 2017, **5**, 1334–1347.
- 13 X. Q. Kong, E. Scott, W. Ding, J. A. Mason, J. R. Long and J. A. Reimer, *J. Am. Chem. Soc.*, 2012, **134**, 14341–14344.
- 14 H. Lyu, O. I. F. Chen, N. Hanikel, M. I. Hossain, R. W. Flraig, X. K. Pei, A. Amin, M. D. Doherty, R. K. Impastato, T. G. Glover, D. R. Moore and O. M. Yaghi, *J. Am. Chem. Soc.*, 2022, **144**, 2387–2396.



15 H. Lyu, H. Z. Li, N. Hanikel, K. Y. Wang and O. M. Yaghi, *J. Am. Chem. Soc.*, 2022, **144**, 12989–12995.

16 T. M. McDonald, J. A. Mason, X. Q. Kong, E. D. Bloch, D. Gygi, A. Dani, V. Crocella, F. Giordanino, S. O. Odoh, W. S. Drisdell, B. Vlaisavljevich, A. L. Dzubak, R. Poloni, S. K. Schnell, N. Planas, K. Lee, T. Pascal, L. W. F. Wan, D. Prendergast, J. B. Neaton, B. Smit, J. B. Kortright, L. Gagliardi, S. Bordiga, J. A. Reimer and J. R. Long, *Nature*, 2015, **519**, 303–308.

17 J. B. Lin, T. T. T. Nguyen, R. Vaidhyanathan, J. Burner, J. M. Taylor, H. Durekova, F. Akhtar, R. K. Mah, O. Ghaffari-Nik, S. Marx, N. Fylstra, S. S. Iremonger, K. W. Dawson, P. Sarkar, P. Hovington, A. Rajendran, T. K. Woo and G. K. H. Shimizu, *Science*, 2021, **374**, 1464–1469.

18 Y. Zhou, J. L. Zhang, L. Wang, X. L. Cui, X. L. Liu, S. S. Wong, H. An, N. Yan, J. Y. Xie, C. Yu, P. X. Zhang, Y. H. Du, S. B. Xi, L. R. Zheng, X. Z. Cao, Y. J. Wu, Y. X. Wang, C. Q. Wang, H. M. Wen, L. Chen, H. B. Xing and J. Wang, *Science*, 2021, **373**, 315–320.

19 C. Jia, R. R. Liang, S. X. Gan, S. Y. Jiang, Q. Y. Qi and X. Zhao, *Chem. - Eur. J.*, 2023, **29**, e202300186.

20 Y. F. Zeng, R. Q. Zou and Y. L. Zhao, *Adv. Mater.*, 2016, **28**, 2855–2873.

21 X. Zhao, Y. X. Wang, D. S. Li, X. H. Bu and P. Y. Feng, *Adv. Mater.*, 2018, **30**, 1705189.

22 C. E. Bien, K. K. Chen, S. C. Chien, B. R. Reiner, L. C. Lin, C. R. Wade and W. S. W. Ho, *J. Am. Chem. Soc.*, 2018, **140**, 12662–12666.

23 C. E. Bien, Q. Liu and C. R. Wade, *Chem. Mater.*, 2020, **32**, 489–497.

24 A. Kumar, C. Hua, D. G. Madden, D. O’Nolan, K. J. Chen, L. A. J. Keane, J. J. Perry and M. J. Zaworotko, *Chem. Commun.*, 2017, **53**, 5946–5949.

25 Z. Q. Zhang, Q. Ding, J. Y. Cui, X. L. Cui and H. B. Xing, *Sci. China Mater.*, 2021, **64**, 691–697.

26 M. D. Jiang, B. Li, X. L. Cui, Q. W. Yang, Z. B. Bao, Y. W. Yang, H. Wu, W. Zhou, B. L. Chen and H. B. Xing, *ACS Appl. Mater. Interfaces*, 2018, **10**, 16628–16635.

27 P. Nugent, Y. Belmabkhout, S. D. Burd, A. J. Cairns, R. Luebke, K. Forrest, T. Pham, S. Q. Ma, B. Space, L. Wojtas, M. Eddaoudi and M. J. Zaworotko, *Nature*, 2013, **495**, 80–84.

28 W. Liang, P. M. Bhatt, A. Shkurenko, K. Adil, G. Mouchaham, H. Aggarwal, A. Mallick, A. Jamal, Y. Belmabkhout and M. Eddaoudi, *Chem.*, 2019, **5**, 950–963.

29 P. M. Bhatt, Y. Belmabkhout, A. Cadiau, K. Adil, O. Shekhah, A. Shkurenko, L. J. Barbour and M. Eddaoudi, *J. Am. Chem. Soc.*, 2016, **138**, 9301–9307.

30 O. Shekhah, Y. Belmabkhout, Z. J. Chen, V. Guillerm, A. Cairns, K. Adil and M. Eddaoudi, *Nat. Commun.*, 2014, **5**, 4228.

31 Z. Q. Zhang, Q. Ding, S. B. Peh, D. Zhao, J. Y. Cui, X. L. Cui and H. B. Xing, *Chem. Commun.*, 2020, **56**, 7726–7729.

32 L. A. Darunte, A. D. Oetomo, K. S. Walton, D. S. Sholl and C. W. Jones, *ACS Sustainable Chem. Eng.*, 2016, **4**, 5761–5768.

33 S. Choi, T. Watanabe, T. H. Bae, D. S. Sholl and C. W. Jones, *J. Phys. Chem. Lett.*, 2012, **3**, 1136–1141.

34 A. J. Emerson, A. Chahine, S. R. Batten and D. R. Turner, *Coord. Chem. Rev.*, 2018, **365**, 1–22.

35 R. L. Siegelman, P. J. Milner, A. C. Forse, J. H. Lee, K. A. Colwell, J. B. Neaton, J. A. Reimer, S. C. Weston and J. R. Long, *J. Am. Chem. Soc.*, 2019, **141**, 13171–13186.

36 P. Q. Liao, X. W. Chen, S. Y. Liu, X. Y. Li, Y. T. Xu, M. N. Tang, Z. B. Rui, H. B. Ji, J. P. Zhang and X. M. Chen, *Chem. Sci.*, 2016, **7**, 6528–6533.

37 R. L. Siegelman, T. M. McDonald, M. I. Gonzalez, J. D. Martell, P. J. Milner, J. A. Mason, A. H. Berger, A. S. Bhowm and J. R. Long, *J. Am. Chem. Soc.*, 2017, **139**, 10526–10538.

38 J. S. A. Carneiro, G. Innocenti, H. J. Moon, Y. Guta, L. Proano, C. Sievers, M. A. Sakwa-Novak, E. W. Ping and C. W. Jones, *Angew. Chem., Int. Ed.*, 2023, **62**, e202302887.

39 S. C. Li, M. R. Ceron, H. V. Eshelman, A. J. Varni, A. Maiti, S. Akhade and S. H. Pang, *ChemSusChem*, 2023, **16**, e202201908.

40 H. Furukawa, F. Gandara, Y. B. Zhang, J. C. Jiang, W. L. Queen, M. R. Hudson and O. M. Yaghi, *J. Am. Chem. Soc.*, 2014, **136**, 4369–4381.

41 H. Dong, G. Yang, X. Zhang, X. Meng, J. Sheng, X. Sun, Y. Feng and F. Zhang, *Chem. - Eur. J.*, 2018, **24**, 17148–17154.

42 D. L. Fu, Y. Park and M. E. Davis, *Angew. Chem., Int. Ed.*, 2022, **61**, e202112916.

